ADVANCED ELECTRONIC MATERIALS
www.advelectronicmat.de

PEDOT:PSS Microchannel-Based Highly Sensitive Stretchable Strain Sensor

*Mitradip Bhattacharjee, Mahesh Soni, Pablo Escobedo, and Ravinder Dahiya**

This paper presents poly(3,4-ethylenedioxythiophene) polystyrene sulfonate polymer microchannel (diameter ≈175 µm) based stretchable strain sensor developed inside polydimethylsiloxane substrate. The microchannel diameter changes when subjected to various strains, leading to change in the resistance of strain sensor. The sensor exhibits about three order ($\Delta R/R_0 \approx 1200$) increase in the resistance (R) for 10% applied strain ($\Delta L/L$, L = length of the sensor). This leads to a gauge factor (GF $\Delta(\Delta R/R_0)/(\Delta L/L)$ of ≈12 000, which is about ≈400 times higher than most of the reported polymer-based strain sensors. The sensor is evaluated up to a maximum strain of 30%, which is the standard strain limit associated with human body parts such as fingers and wrists. The sensor exhibits a considerably good average degree of hysteresis (<9%). Further, the sensor is also studied for bending and twisting experiments. A response of ($\Delta R/R_0 \approx 250$) and ($\Delta R/R_0 \approx 300$) is recorded for 90° bending and 150° twisting, respectively. The sensor shows an electrical resolution of ≈150% per degree of free bending and ≈12k% per percentage of stretching. Finally, the potential application of presented sensor in robotics and wearable systems is demonstrated by using sensor feedback from human hand to remotely control the robotic hand movements.

1. Introduction

Several applications such as wearable electronics,[1] human–machine interface,[2] robotics and prosthesis,[3] and human activity monitoring[4] require measurement of mechanical deformation and strain. Strain sensors are important for the applications that experience bending, for example, in prosthesis and robotics applications, where strain sensors could monitor and control the bending of hand joints, fingers, etc.[5] Similarly, strain sensing is also very important in wearable and flexible electronics, in order to monitor or detect the damaged interconnects due to frequent bending.[6] The advent of flexible and wearable sensor system facilitates the monitoring of different physiological parameters[7] harnessing energy-autonomous solutions.[8]

A variety of transduction mechanisms have been implemented for the measurement of strain. The most explored techniques are resistive/piezoresistive,[9] strain gauges,[10] capacitive,[11] optical fiber,[12] and piezoelectric.[13] Among these, resistive strain sensors are most frequently used owing to its advantages in fabrication, operation, and calibration processes. In resistive strain sensor the geometrical deformation of the active material with applied strain results in the corresponding change in the electrical resistance. The sensitivity of a strain sensor is defined as gauge factor (GF) which is defined as the ratio of percentage change of sensor response to the applied strain. The metal-foil strain gauges[14] show low values of GF (<5) whereas the semiconductor-based piezoresistive sensors[15] have high values (<200) of GF. A number of previously reported strain and stress sensors are based on nanostructured materials such as carbon nanotubes (CNTs),[16] nanoparticles,[17] and nanowires.[18] Most of these devices exhibit piezoresistive properties, thus showing a change in the electrical conductance when the material undergoes a small strain.[19] Apart from these, conductive polymer-based strain sensors have been also reported recently.[20] Among them the conductive poly(3,4-ethylenedioxythiophene) polystyrene sulfonate (PEDOT:PSS) has gained significant attention owing to its good electrical and structural properties.[21] The PEDOT:PSS-based strain sensors are mostly printed between the two electrodes. However, these sensors suffer from environmental effects such as excessive use, temperature, humidity, etc. Of late, microchannel based strain sensors have been developed using 3D-printed techniques.[22] However, the fabrication of a series of uniform microchannels with an economical process is a bottleneck in using these for affordable sensor development. In this direction, our previous work[23] on a stretchable strain sensor based on CNT is relevant as dielectrophoresis (DEP) technique was employed to fabricate the sensors.

In this paper, we present a microchannel based strain sensor. At least two order change in resistance was observed across the fabricated sensor for an applied strain up to 30%. The presented sensor is developed using a simple fabrication technique

Dr. M. Bhattacharjee[+], Dr. M. Soni, Dr. P. Escobedo, Prof. R. Dahiya
Bendable Electronics and Sensing Technologies (BEST) Group
University of Glasgow
Glasgow G12 8QQ, UK
E-mail: Ravinder.Dahiya@glasgow.ac.uk

The ORCID identification number(s) for the author(s) of this article can be found under https://doi.org/10.1002/aelm.202000445.

[+]Present address: Electrical Engineering and Computer Science, Indian Institute of Science Education and Research (IISER) Bhopal, MP 462066, India

© 2020 The Authors. Published by WILEY-VCH Verlag GmbH & Co. KGaA, Weinheim. This is an open access article under the terms of the Creative Commons Attribution License, which permits use, distribution and reproduction in any medium, provided the original work is properly cited.

DOI: 10.1002/aelm.202000445

without requiring any external power or dedicated arrangement for deposition of materials/contacts with ten times superior performance. We present the theoretical basis of strain sensing and comparison with the experimental results, as well as evaluate the effect of bending and twisting on the strain measurements. Furthermore, the application of the presented sensor has been demonstrated in terms of closed-loop control of a 3D-printed robotic hand. In our previous study, the percentage strain and maximum change in response were taken into consideration,[24] however, here a detailed analysis has been performed, and the fraction strain values and the average change in resistance were considered for the analysis. We observed about three order ($\Delta R/R_0 \approx 1200$) increase in the average resistance (R) value for 10% applied strain ($\Delta L/L$, L = length of sensor). This leads to a gauge factor (GF = $(\Delta R/R_0)/(\Delta L/L)$ of ≈12 000, which is significantly better (≈400 times) than most of the reported polymer[25] and other resistive[26] strain sensors as discussed later in Table S1 in the Supporting Information. Gauge factor represents the sensitivity of a strain sensor and thus higher GF indicates a highly sensitive sensor. Apart from this, the proposed sensor showed good linearity up to its maximum starching limit, good resolution in both stretching and bending condition, sufficient dynamic range, and nice stability as discussed later in the paper.

2. Experimental Section

2.1. Materials

Polydimethylsiloxane (PDMS) was purchased from Sigma Aldrich, and the conductive polymer PEDOT:PSS was procured from Merck, UK. The chemicals were of analytical grade and were used as procured without further purification. The electronic components were purchased from RS Components, UK.

2.2. Fabrication

Transparent polymer PDMS was used to fabricate the strain sensor. In this case, the microchannel was fabricated using the replica molding technique.[27] In this process, a 10:1 mixture of the PDMS and the cross-linker was prepared and mixed properly using a glass rod. The prepared mixture was then degassed for 1 h in vacuum desiccator to ensure that no air bubble was trapped in the mixture. Thereafter, the mixture was poured inside a circular mold of diameter 5.5 cm. A metal wire (diameter ≈275 µm) was used in the mold to create the channel inside the PDMS. The mold was then dried in a convection

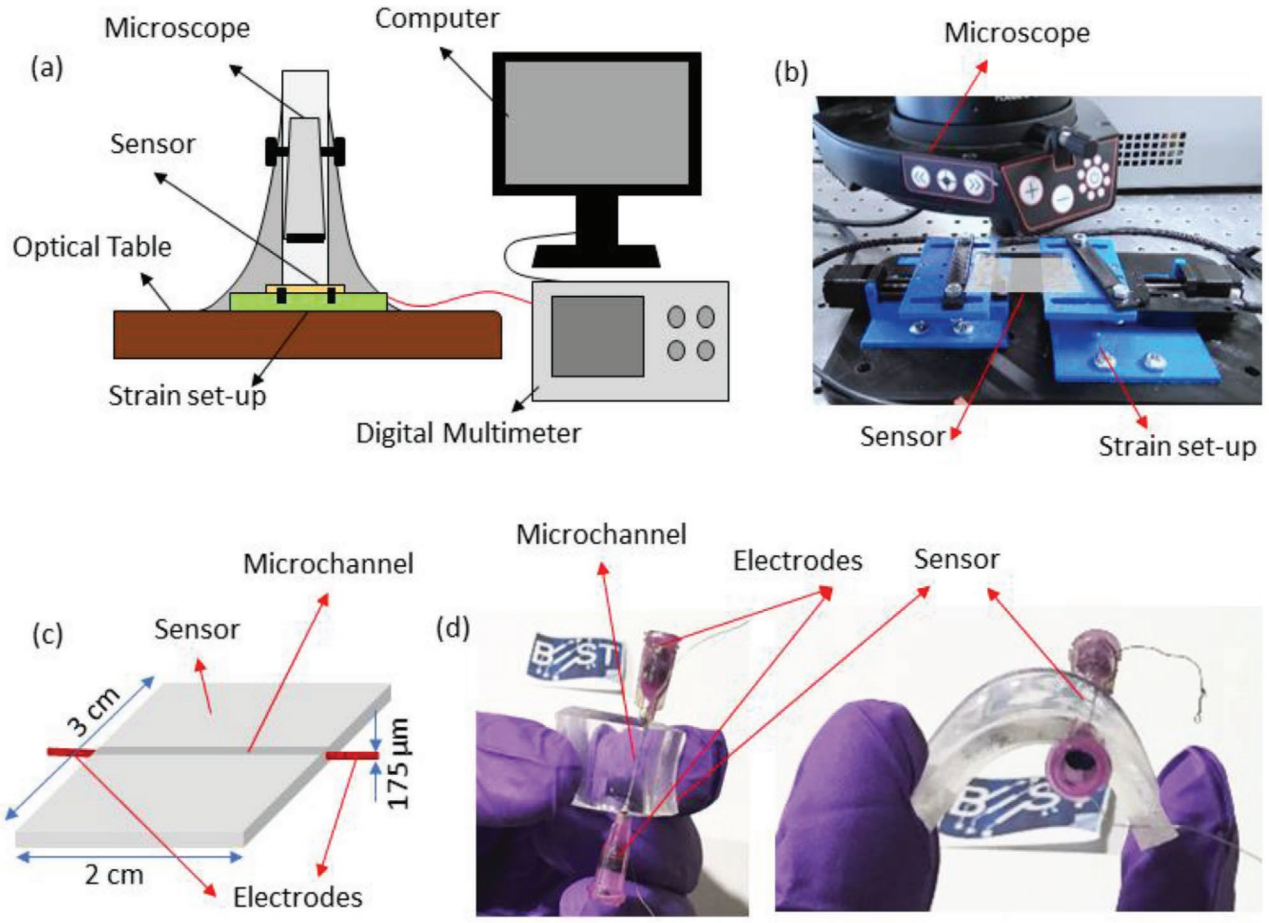

Figure 1. a) The schematic illustration of the experimental setup; b) the real image of the strain setup employed in the experiments; c) the schematic illustration of the fabricated strain sensor; d) the optical image of the flexible sensor.

 © 2020 The Authors. Published by WILEY-VCH Verlag GmbH & Co. KGaA, Weinheim

oven for 2 h at 70 °C. After drying, the hard PDMS was taken out of the mold and the wire was taken out of the PDMS to form the channel. Thereafter, a syringe was used to inject conducting liquid polymer PEDOT:PSS into the microchannel. The PDMS block was then dried for another 3 h at 70 °C. The process of injection and curing was repeated three times. The optimization was done by measuring the electrical resistance of the sensor each time after the injection and curing cycle. After this, the fabricated sensor was cut into a rectangular shape of dimension (3 cm × 2 cm) for further experiments. Commercially available cylindrical Al electrodes with diameter ≈275 µm were then inserted to both ends of the microchannel for electrical connections. A gap of ≈1.5 mm was kept inside the microchannel between the two electrodes. The suitable thickness of the sensor was found to be ≈3.1 mm. A discussion is added in Section SI and Figure S1a,b of the Supporting Information. The schematic illustration and real images of the experimental setup and sensor are shown in **Figure 1**a–d.

2.3. Characterization

The strain was applied to the sensor using a LabVIEW controlled strain generation setup, and the electrical characterization was performed using a digital multimeter (Agilent 34461A). The strain generation setup has two holders which are able to move back and forth to generate uniaxial strain with controllable velocity in the sensor, as illustrated in Figure 1a,b. The sensor was attached to the setup using the holders and thin metallic wires were used to make the electrical connections. A maximum of 30% strain was applied with a velocity of V_S = 0.1, 0.25, and 0.75 mm s^{-1} (i.e., strain rates 3.3 × 10^{-3}, 8.3 × 10^{-3}, and 25 × 10^{-3}% s^{-1}, respectively). The strain sensor was tested for up to 30% of strain, which is the standard strain limit associated with human skin at different body parts such as fingers, wrists, knee, and elbows for the collagen fibers and tissues to become straitened.[28] The measurement setup is illustrated in Figure 1a,b, where image (a) shows the schematic of the experimental setup and image and image (b) shows the real image of the strain generation setup. The schematic diagram and real image of the sensor are shown in Figure 1c,d, respectively. The initial experiment was performed for 10% strain with a velocity of 0.1 mm s^{-1} as illustrated in **Figure 2**a. Three order ($\Delta R/R_0 \approx 1200$) changes were observed in electrical resistance. The base resistance, in this case, was ≈140 Ω and the resistance at the highest strain was ≈180 kΩ. The results are further discussed in detail later in Section 3. However, the reason behind the change in resistance was the formation of defects and electrical discontinuities in the polymer as discussed in the following section.

3. Results and Discussions

3.1. Strain Sensor Characterization

The resistance (R_S) value across the sensor was measured as the sensor response. The response of the sensor for a maximum of 10% dynamic applied strain at a speed of V_S = 0.1 mm s^{-1}

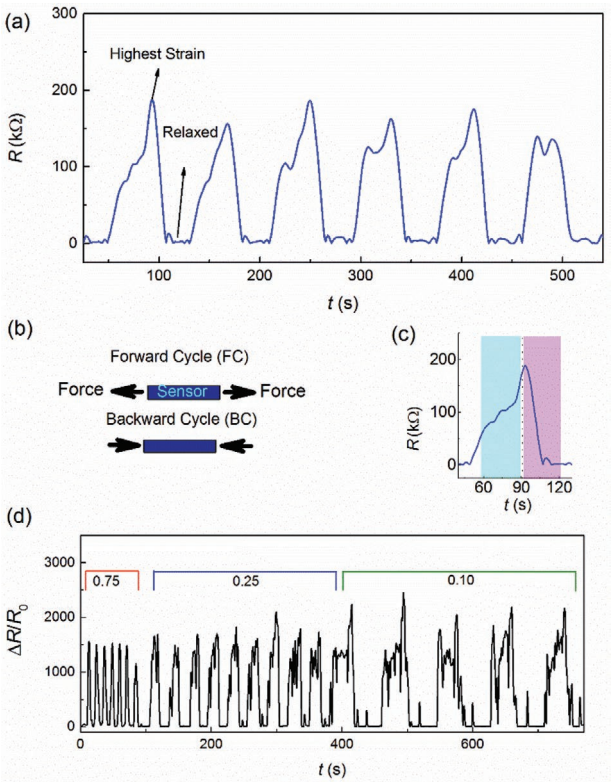

Figure 2. a) Sensor response under a strain of 10% at 0.1 mm s^{-1} velocity; b) the schematic illustration of forward (FC) and backward cycle (BC); c) the single cycle of forward and backward movement; d) response of the sensor at different velocity (0.1, 0.25, and 0.75 mm s^{-1}) of applied strain.

is illustrated in Figure 2a. The resistance across the sensor increased with the strain and then reduced back to its initial resistance with a decrease in the strain value, as illustrated in Figure 2a. Figure 2b shows the forward cycle (FC), i.e., increase in the strain and backward cycle (BC), i.e., decrease in the strain schematically. Figure 2c illustrates one complete cycle consisting of a forward and backward cycle. It is interesting to see that the recovery of the sensor is faster as compared to the forward cycle. The reason behind this response could be the faster rearrangement of polymer material inside the closed microchannel structure in the backward movement. In this situation, the PEDOT:PSS polymer rearranges back due to the contraction of the sensor to its initial position faster to produce more conductive paths. In case of small deformation, polymer materials hold the memory of the initial positions due to their inherent elastic nature.[29] The sensor was also tested for different speeds of applied strain in the quasistatic and medium range (generally the case in real-life systems).[30] Figure 2d shows the response of the sensor at different speeds (0.1, 0.25, 0.75 mm s^{-1}) of applied strain, which corresponds to a strain rate between 0.3% and 2.5% s^{-1}. The sensor showed a stable response for these velocity values.

The strain response of the sensor is shown in **Figure 3**. Figure 3a shows the image of the sensor at different stretching levels. The sensor showed a significant change in the response as illustrated in Figure 3a,b. Figure 3a shows the temporal response of sensor under a strain of 10%, 20%, and 30% at a

© 2020 The Authors. Published by WILEY-VCH Verlag GmbH & Co. KGaA, Weinheim

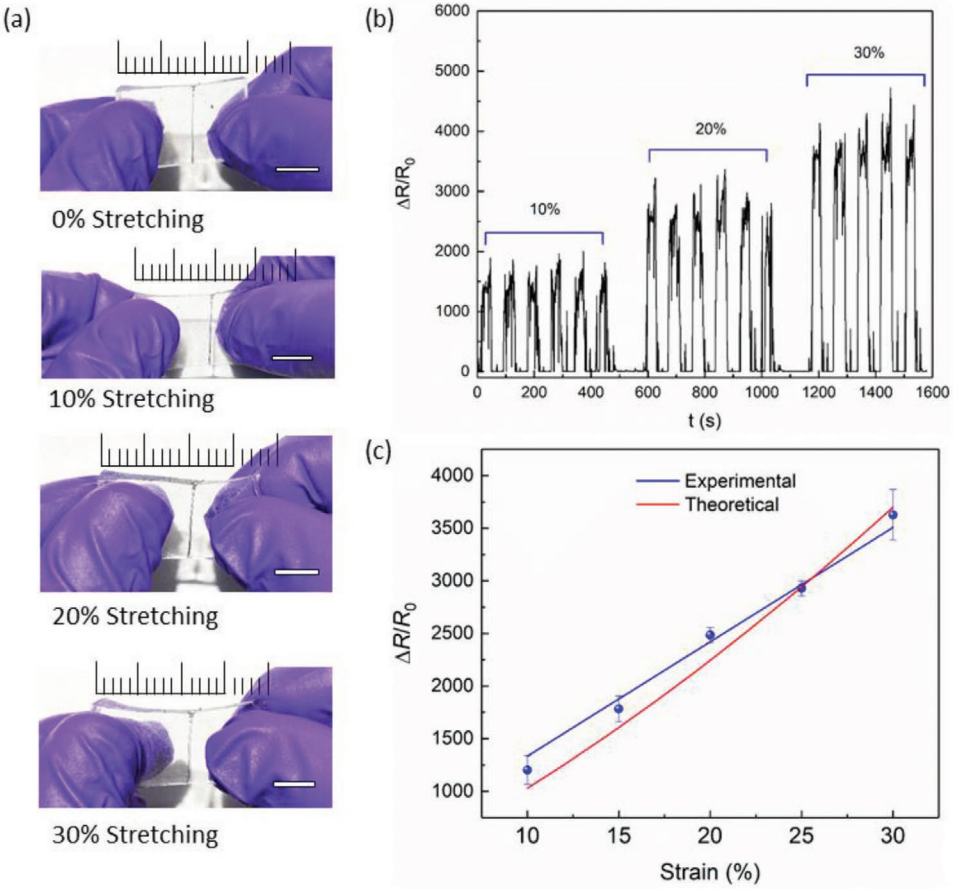

Figure 3. a) Optical images of the sensor at different stretching levels; b) temporal response of sensor under a strain of 10%, 20%, and 30% at a rate of 0.1 mm s^{-1} velocity; c) the response of the sensor (experimental and theoretical) for different strain values.

rate of 0.1 mm s^{-1} velocity and Figure 3b shows both the experimental and theoretical response of the sensor for different strain values. The experimental values are in good agreement with the theoretical one as illustrated in Figure 3b. The theoretical study is described in the following section to understand the mechanism. The experimental reason of the strain sensing is described in Section SI of the Supporting Information. Figure S1c–h (Supporting Information) describes the sensor under relaxed and strained condition with optical and electron microscopic images.

3.2. Strain Sensing Mechanism

The electrical conductivity of a composite material depends on the volumetric fraction of the defects and the percolation threshold.[31] Mathematically, this can be defined as $\sigma \propto (V_f - V_c)^s$, where σ is the electrical conductivity, V_f and V_c are the volumetric fraction of the material and the critical volumetric fraction of the filler, respectively. The variable s is the fitting parameter, which is used to best fit the experimental data. In this case, the deformation of the channel reduces the effective volume fraction of the PEDOT:PSS inside the channel due to the formation of electrical discontinuities and defects which lead to the reduction of the conductive path inside the channel. This can be explained by the electrical percolation mechanism. Electrical percolation defines a transition of material from one electrical property to the other (e.g., transition from conductor to insulator).[32] In most of the cases, the composite materials are considered to be the best case for this analysis. However, the geometrical deformation that creates void and electrical discontinuities in a soft material is considered on this occasion. Effectively, in such a scenario the volume fraction of the material changes similar to a composite material.

Considering the PEDOT:PSS is uniformly distributed in the PDMS microchannel, the areal fraction of PEDOT:PSS will be equal to the volumetric fraction of the materials, i.e., $V_f = D_f$ and $V_c = D_c$, where D_f and D_c are the corresponding areal fraction values. In this case, the resistance of the sensor increases with the increase in applied strain (Figure 3a,b) due to the expansion of microchannel (Figure S1c–f, Supporting Information). The volume fraction of the material changes as it creates void spaces due to the formation of electrical discontinuities. The electrical conductivity, in this case, becomes $\sigma \propto (D_f - D_c)^s$. Since the resistance and conductivity are inversely proportional (i.e., $R = (1/\sigma)\ (l/A)$, where l is the length of the conductor and A is the cross-sectional area), the relation between R and the D_f and D_c will be $R \propto (D_f - D_c)^{-s}$.

In our experiment, the effective length of the channel was 1.5 mm and the diameter of the microchannel is 175 µm

© 2020 The Authors. Published by WILEY-VCH Verlag GmbH & Co. KGaA, Weinheim

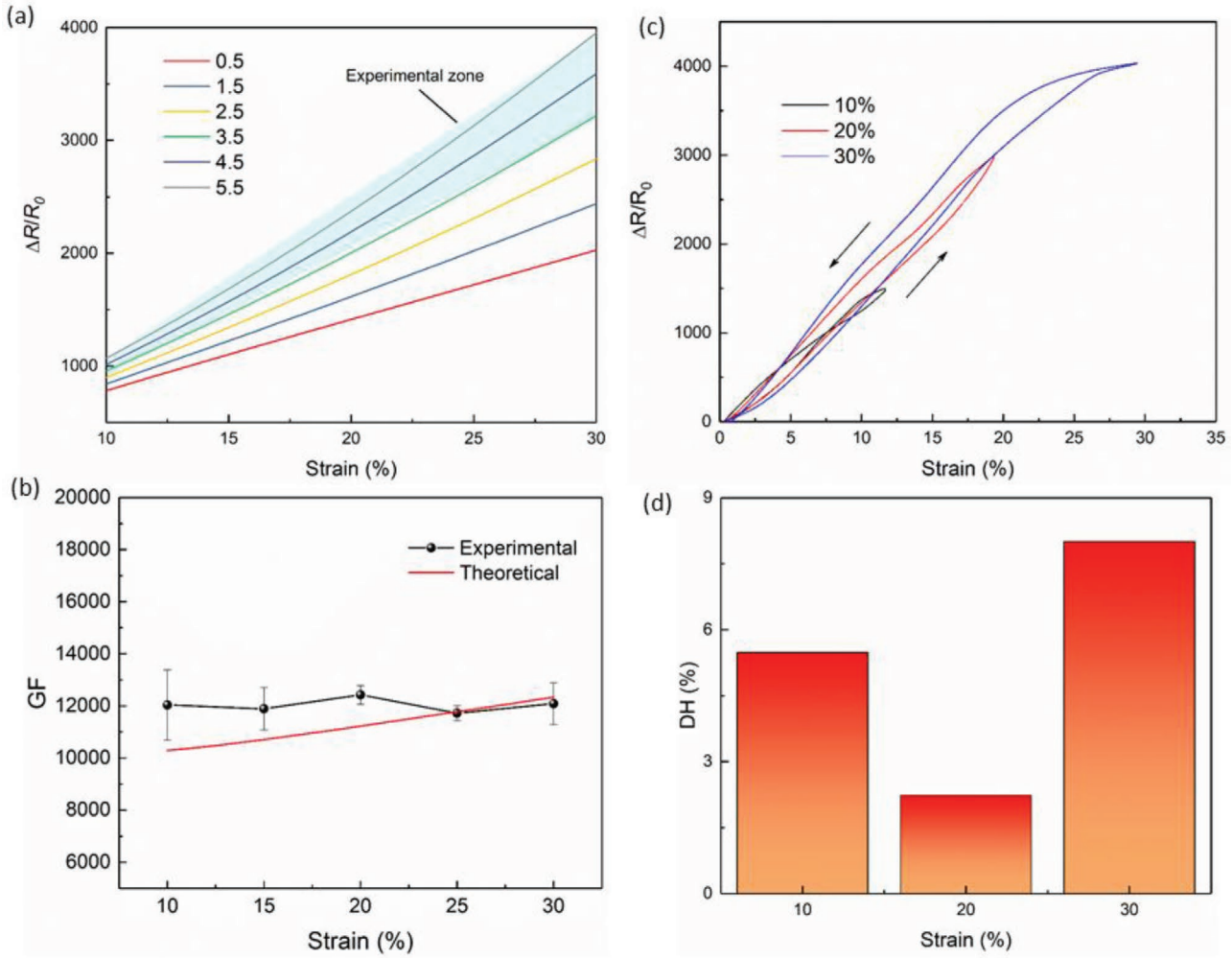

Figure 4. a) Response of the sensor simulated for different values of m; b) gauge factor (GF) (experimental and simulated) of the strain sensor for different strain values; c) hysteresis curve of the fabricated strain sensor for different maximum strain values; d) the average degree of hysteresis (DH) values for different maximum strain values.

(Figure S1e, Supporting Information). The change in the areal fraction D_f depends primarily on two factors: the number of electrical discontinuities in the system (N) and the magnitude of percentage strain ($\gamma = (\Delta L/L) \times 100$) in the sensor. Further, N is also a function of γ. In low strain region, a linear relation[33] between N and γ is considered, $N = m\gamma + N_0$. The N_0 represents the initial electrical discontinuities present in the system, which is negligible compared to the electrical discontinuities formed after the applied strain and m is the proportionality constant that determines the formation of electrical discontinuities in low strain region. Higher the value of m, higher is the crack formation for the same strain value. Here, m can be defined as $m = (E_1 \times A_1)/(E_2 \times A_2)$, where E_1 is the young's modulus of active material (i.e., PEDOT:PSS) and A_1 is the cross-section of the channel, respectively, and E_2 and A_2 are the same parameters for embedded material (i.e., PDMS). In this case, the percolation threshold was determined by considering the formation of electrical discontinuities on the PEDOT:PSS using the formula, $D_c = V_c = (\pi r^2 L)/(8\pi r^2 L + \pi r L^2)$, where L and r are the length and radius of the discontinuities, respectively. The typical values of the same were calculated from the FESEM micrograph (Figure S1g,h, Supporting Information) of the same. The theoretical results are in good agreement with the experimental values, as shown in Figure 3b.

The theoretical study shows that the response of the sensor will be higher if the active material has a higher elastic modulus. This is assuming the same geometrical structure for the embedding material. Thus, a higher m value gives a higher response as illustrated in **Figure 4**a. The value of m for the materials used ranges between 4.5 and 5.5 indicated as an experimental zone in the plot. Further, the GF was also measured for the proposed sensor and it was also in line with the simulated result as shown in Figure 4b. The value of GF is considerably high (≈12 000) compared to other polymer counterparts. Table S1 in the Supporting Information shows the performance comparison between the presented sensor and different flexible strain sensors reported in the literature as stated before. Further, experimental studies were performed for hysteresis study. Figure 4c shows the hysteresis of the fabricated microchannel based strain sensors for different

© 2020 The Authors. Published by WILEY-VCH Verlag GmbH & Co. KGaA, Weinheim

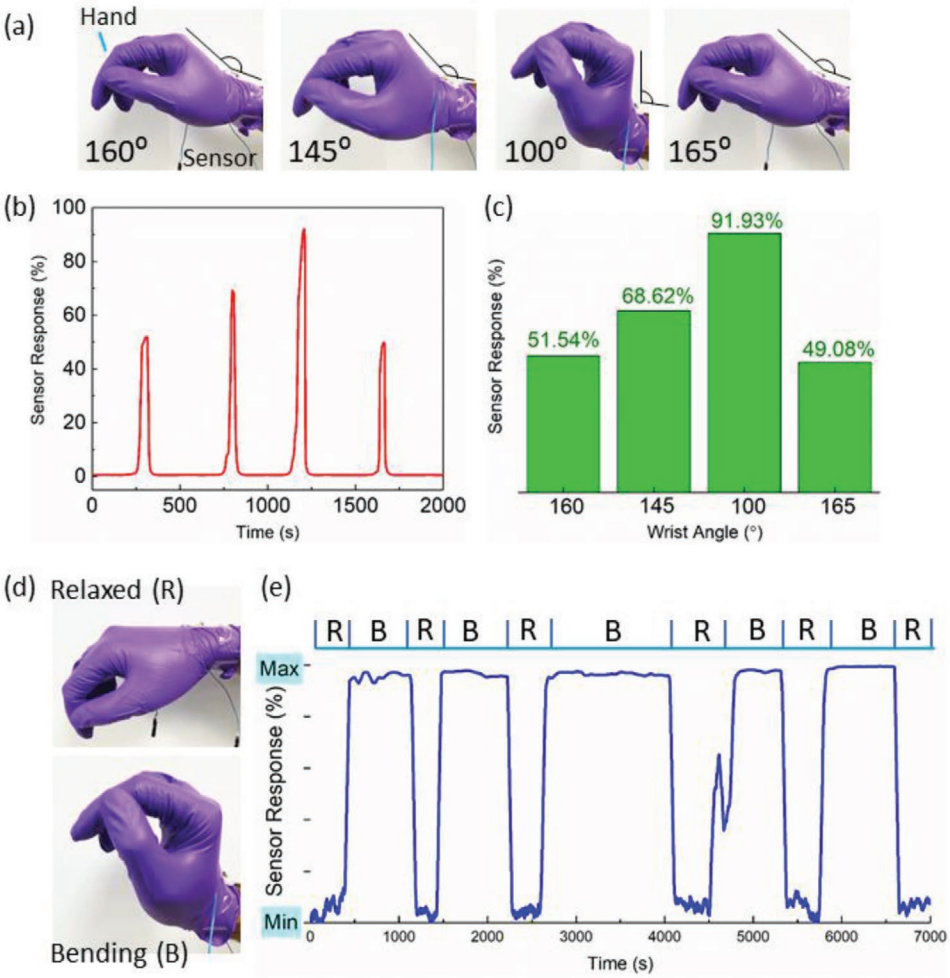

Figure 5. a) optical image of the hand bent at different angles; b) the temporal response of the sensor due to the bending; c) response of the sensor for different bending angles; d) experimental condition of relaxed (R) and bending (B) condition; e) temporal response of the sensor for different holding times at maximum bending (B) condition.

maximum strain values. The average degree of hysteresis (DH) is calculated[34] using, DH = $(|A_L - A_U|/A_L) \times 100\%$, where A_L and A_U are the area under loading and unloading curves, respectively. The DH value is obtained for different strain values (10%, 20%, and 30%) as illustrated in Figure 4d and it is in the range of <9%, which is considerably good. Further, the sensor was tested for different bending and twisting conditions and it was found that they are more responsive for higher bending angles as described in Section SIII of the Supporting Information. Figure S2 (Supporting Information) illustrates the bending and twisting results of the presented strain sensor. Further, a stability and multiple cycle testing of the sensor was also performed as shown in Figure S3 of the Supporting Information.

3.3. Application of the Strain Sensor

The sensor was further tested on human and robotic hands after connecting with a system. The sensor response from the system is demonstrated in **Figures 5** and **6**. Figure 5 shows the response of the sensor for wrist movements when it was fixed with a human wrist using a nitrile glove. The sensor was fixed using a double-sided adhesive tape and then it was connected to a LabVIEW program using a microcontroller-based acquisition circuit (for further details, see Section SIV of the Supporting Information). The response of the sensor, in this case, was from the designed circuit, which is calibrated as per previously reported results (Figures 2 and 3) in this paper. In this case, the response of the maximum stretched condition for this application corresponds to the 100% response of the sensor. Figure 5a shows the optical image of the experimental condition, placement of the sensor and wrist positions. The corresponding temporal response and the response at different angles are illustrated in Figure 5b,c, respectively. Further, an experiment was also performed at relaxed (R) and bent (B) condition of the wrist as shown in Figure 5d at different holding time, i.e., holding the wrist at the bent condition for different time periods to check the holding response of the sensor. Figure 5e shows the response of the sensor was quite stable in this condition. A demonstration was performed as shown in Video S1 (Supporting Information).

© 2020 The Authors. Published by WILEY-VCH Verlag GmbH & Co. KGaA, Weinheim

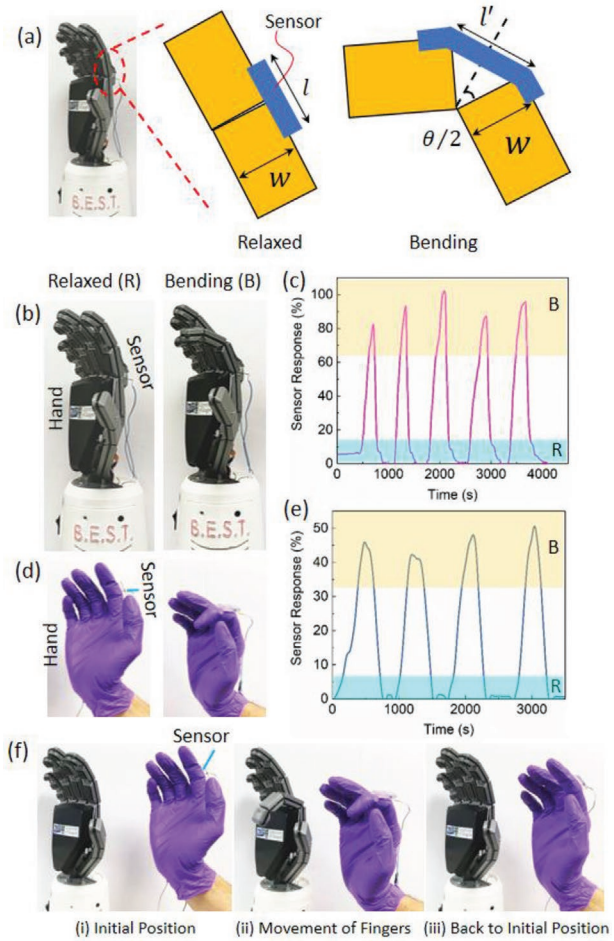

Figure 6. a) schematic representation of sensor stretching due to the bending of the finger; b) optical image of the robotic hand with the index finger relaxed (R) and bending (B) condition; c) temporal response of the sensor due to bending of the finger; d) optical image of the human hand with the index finger relaxed (R) and bending (B) condition; e) temporal response of the sensor due to bending of the finger; f) the optical images of the three steps of the demonstration where the sensor attached in the human finger was taken as feedback to move the robotic finger.

Further, in order to check the feedback control of the sensing system, experiments were also performed with a 3D-printed robotic hand.[35,36] The robotic hand and wrist were designed using the computer-aided-design (CAD) software SolidWorks 2018 SP4.0 (Dassault Systems, Vélizy-Villacoublay, France). The hand design was based on the average size of an adult male. The palm is 85 mm wide, 120 mm long, and 30 mm thick. In the palm region, there are cavities for the fingers' actuators (PQ12-63-6-R microlinear actuator, Actuonix). More details can be found in a previous publication of our group.[36] In this case, initially separate experiments were done by attaching the presented strain sensor on human finger and robotic finger. The calibration of the system was performed using the stretching experiment. The sensor was fixed in the joints of the phalanges of robotic and human finger using a double-sided and single-sided adhesive tape. Hence, a bending of angle θ as shown in Figure 6a schematically, would lead to stretching of, $\Delta l = l' = 2w \sin(\theta/2)$, where l is the length of the sensor and w is the width of the robotic finger. Hence, the correlation between the bending angle, θ and stretching, $\Delta l/l$ can be calculated using, $\Delta l/l = l'/l = (2w \sin(\theta/2))/l$. Figure 6b,d shows the optical image of the robotic and human hand with the sensor attached in index finger in relaxed (R) and bent (B) condition, respectively. The corresponding response of the sensor from the system is shown in Figure 6c,e, respectively. The demonstration of the experiment with the robotic hand is shown in Video S2 (Supporting Information). Further, an experiment was performed where the response of the sensor attached in the human finger was taken as feedback to move the robotic finger. Figure 6f shows the optical images of the three steps of this demonstration. The demonstration is shown in Video S3 (Supporting Information). Details of the circuit are discussed in Section SIV of the Supporting Information. Figure S4 (Supporting Information) shows the circuit associated with these experiments. The resolution can be extracted from the experiments performed with real hand and robotic hand. It was observed from the free bending experiments that the electrical bending resolution was 150% per degree of free bending. However, in case of bending experiments with robotic hand the end of the sensor was attached with the finger and thus upon bending the sensor underwent axial strain and thus the resolution in that case was quite higher and similar to starching as discussed later. Under that condition, a bending of ≈2.7° can be realized using the fabricated sensor as per experiments with a proper circuit arrangement as discussed. The electrical resolution for stretching is quite high ≈12k% per percentage of stretching.

The presented sensor was highly sensitive (GF ≈ 12 000) and shows good performance as demonstrated with human and robotic hand. **Figure 7** shows the graphical representation of the GF with maximum strain value and illustrates where the proposed strain sensor lies compared to prior art. It is clear from Figure 7 that the proposed sensor has at least ≈400-fold higher sensitivity compared to most of the reported resistive strain sensors. Moreover, it showed significantly high sensitivity among resistive polymer strain sensors reported so far. Further, the proposed sensor shows good linearity up to its maximum starching limit, good resolution in both stretching and bending condition, sufficient dynamic range, and nice stability.

4. Conclusions

A microchannel based ultrasensitive strain sensor was developed using conductive PEDOT:PSS in PDMS microchannel to measure the strain cycle. The microchannel was fabricated using the replica molding technique with a channel diameter of 175 µm. The response of the sensor was based on the change of electrical resistance due to the variation of effective dimension which creates defects and electrical discontinuities in the polymer upon the applied strain. A theoretical analysis was carried out and compared with the experimental results. We observed about three order ($\Delta R/R_0 \approx 1200$) increase in the resistance (R) value for 10% applied strain ($\Delta L/L$, L = length of the sensor) This lead to a gauge factor (GF = $(\Delta R/R_0)/(\Delta L/L)$ of ≈12 000 for 10% applied strain, which is better (≈400 times) than most of the reported polymer strain sensors. A comparative

© 2020 The Authors. Published by WILEY-VCH Verlag GmbH & Co. KGaA, Weinheim

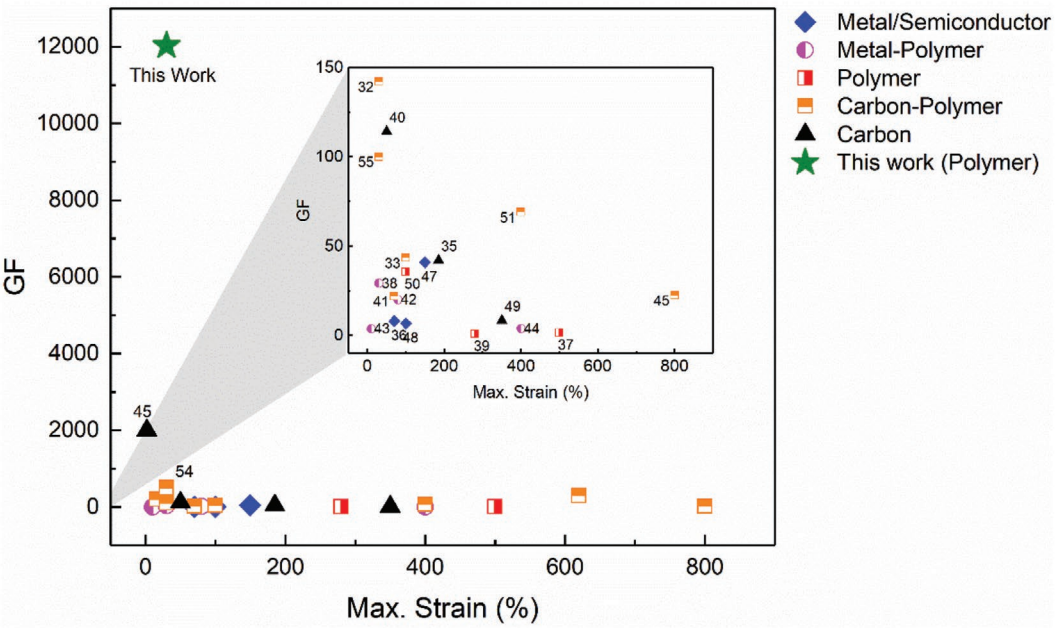

Figure 7. Comparison between previously reported sensors and this work with respect to gauge factor (GF) versus maximum strain values. The numbers corresponding to each data point in the inset indicate the references from which the data have been obtained.

study was also performed and described in the paper. The average degree of hysteresis (DH) was found to be <9% for the maximum strain condition. Further, experiments were also performed for bending and twisting. It was observed that the sensor is also responsive for different bending and twist angles due to the presence of effective strain in these processes. A response of ($\Delta R/R_0 \approx 250$) and ($\Delta R/R_0 \approx 300$) was recorded for 90° bending and 150° twisting. As a proof of concept, the sensor also was demonstrated with human and robotic hand movement. It was also demonstrated that feedback control can be employed with the strain sensor to control a robotic finger movement using human hand.

Supporting Information

Supporting Information is available from the Wiley Online Library or from the author.

Acknowledgements

This work was supported in part by Engineering and Physical Sciences Research Council (EPSRC) through Engineering Fellowship for Growth (EP/R029644/1 and EP/M002527/1), and North West Centre for Advanced Manufacturing (NWCAM) project supported by the European Union's INTERREG VA Programme (H2020-Intereg-IVA5055), managed by the Special EU Programmes Body (SEUPB). The views and opinions in this document do not necessarily reflect those of the European Commission or the Special EU Programmes Body (SEUPB).

Conflict of Interest

The authors declare no conflict of interest.

Author Contributions

The manuscript was written through contributions of all authors. All authors have given approval to the final version of the manuscript.

Keywords

feedback control, gauge factor, microchannels, PEDOT:PSS, strain sensors

Received: April 27, 2020
Published online: July 14, 2020

[1] K. Xu, Y. Lu, S. Honda, T. Arie, S. Akita, K. Takei, *J. Mater. Chem. C* **2019**, *7*, 9609.
[2] K. Sim, Z. Rao, Z. Zou, F. Ershad, J. Lei, A. Thukral, J. Chen, Q.-A. Huang, J. Xiao, C. Yu, *Sci. Adv.* **2019**, *5*, eaav9653.
[3] a) R. Dahiya, N. Yogeswaran, F. Liu, L. Manjakkal, E. Burdet, V. Hayward, H. Jörntell, *Proc. IEEE* **2019**, *107*, 2016; b) M. Soni, R. Dahiya, *Philos. Trans. R. Soc., A* **2020**, *378*, 20190156.
[4] F. Yin, H. Lu, H. Pan, H. Ji, S. Pei, H. Liu, J. Huang, J. Gu, M. Li, J. Wei, *Sci. Rep.* **2019**, *9*, 2403.
[5] R. Dahiya, *Proc. IEEE* **2019**, *107*, 247.
[6] a) A. Kumar, V. Parab, A. Handu, L. Ding, P. Joshi, C. Jiang, S. Sambandan, *Phys. Rev. Appl.* **2019**, *11*, 014057; b) W. Dang, V. Vinciguerra, L. Lorenzelli, R. Dahiya, *Flexible Printed Electron.* **2017**, *2*, 013003.
[7] W. Dang, L. Manjakkal, W. T. Navaraj, L. Lorenzelli, V. Vinciguerra, R. Dahiya, *Biosens. Bioelectron.* **2018**, *107*, 192.
[8] C. García Núñez, L. Manjakkal, R. Dahiya, *npj Flexible Electron.* **2019**, *3*, 1.
[9] Y. Jung, K. Jung, B. Park, J. Choi, D. Kim, J. Park, J. Ko, H. Cho, *Micro Nano Syst. Lett.* **2019**, *7*, 20.
[10] C. Pang, G.-Y. Lee, T.-I. Kim, S. M. Kim, H. N. Kim, S.-H. Ahn, K.-Y. Suh, *Nat. Mater.* **2012**, *11*, 795.

© 2020 The Authors. Published by WILEY-VCH Verlag GmbH & Co. KGaA, Weinheim

[11] A. Frutiger, J. T. Muth, D. M. Vogt, Y. Mengüç, A. Campo, A. D. Valentine, C. J. Walsh, J. A. Lewis, *Adv. Mater.* **2015**, *27*, 2440.
[12] J. Guo, X. Liu, N. Jiang, A. K. Yetisen, H. Yuk, C. Yang, A. Khademhosseini, X. Zhao, S.-H. Yun, *Adv. Mater.* **2016**, *28*, 10244.
[13] R. Sun, B. Zhang, L. Yang, W. Zhang, I. Farrow, F. Scarpa, J. Rossiter, *Appl. Phys. Lett.* **2018**, *112*, 251904.
[14] A. L. Window, *Strain Gauge Technology*, Springer Netherlands, Heidelberg **1992**.
[15] Y. Kanda, *Sens. Actuators, A* **1991**, *28*, 83.
[16] B. M. Lee, K. J. Loh, *Nanotechnology* **2017**, *28*, 155502.
[17] J. Lee, S. Kim, J. Lee, D. Yang, B. C. Park, S. Ryu, I. Park, *Nanoscale* **2014**, *6*, 11932.
[18] S. Shengbo, L. Lihua, J. Aoqun, D. Qianqian, J. Jianlong, Z. Qiang, Z. Wendong, *Nanotechnology* **2018**, *29*, 255202.
[19] J. Sirohi, I. Chopra, *J. Intell. Mater. Syst. Struct.* **2000**, *11*, 246.
[20] a) G. Cai, J. Wang, K. Qian, J. Chen, S. Li, P. S. Lee, *Adv. Sci.* **2017**, *4*, 1600190; b) Y. Zheng, Y. Li, Z. Li, Y. Wang, K. Dai, G. Zheng, C. Liu, C. Shen, *Compos. Sci. Technol.* **2017**, *139*, 64.
[21] J. Eom, J.-S. Heo, M. Kim, J. H. Lee, S. K. Park, Y.-H. Kim, *RSC Adv.* **2017**, *7*, 53373.
[22] a) S. Agarwala, G. L. Goh, Y. L. Yap, G. D. Goh, H. Yu, W. Y. Yeong, T. Tran, *Sens. Actuators, A* **2017**, *263*, 593; b) S. Cheng, Z. Wu, *Adv. Funct. Mater.* **2011**, *21*, 2282; c) D. M. Vogt, Y. Park, R. J. Wood, *IEEE Sens. J.* **2013**, *13*, 4056; d) J. Chossat, T. Yiwei, V. Duchaine, Y. Park, presented at 2015 IEEE Int. Conf. on Robotics and Automation (ICRA), May 2015; e) J. C. Yeo, J. Yu, Z. M. Koh, Z. Wang, C. T. Lim, *Lab Chip* **2016**, *16*, 3244; f) Kenry, J. C. Y , J. Yu, M. Shang, K. P. Loh, C. T. Lim, *Small* **2016**, *12*, 1593; g) Y. Jiao, C. W. Young, S. Yang, S. Oren, H. Ceylan, S. Kim, K. Gopalakrishnan, P. C. Taylor, L. Dong, *IEEE Sens. J.* **2016**, *16*, 7870; h) S. G. Yoon, B. J. Park, S. T. Chang, *Sens. Actuators, A* **2017**, *254*, 1; i) S. Han, C. Liu, H. Xu, D. Yao, K. Yan, H. Zheng, H.-J. Chen, X. Gui, S. Chu, C. Liu, *npj Flexible Electron.* **2018**, *2*, 16; j) N. Cheng, J. H. Low, B. W. K. Ang, A. J. Y. Goh, C. Yeow, *IEEE Sens. J.* **2019**, *19*, 1269.
[23] W. Dang, E. S. Hosseini, R. Dahiya, presented at 2018 IEEE Sensors, October 2018.
[24] M. Bhattacharjee, M. Soni, R. Dahiya, presented at 2019 IEEE Int. Conf. on Flexible and Printable Sensors and Systems (FLEPS), July 2019.
[25] a) M. Wang, K. Zhang, X.-X. Dai, Y. Li, J. Guo, H. Liu, G.-H. Li, Y.-J. Tan, J.-B. Zeng, Z. Guo, *Nanoscale* **2017**, *9*, 11017; b) S. Wang, X. Zhang, X. Wu, C. Lu, *Soft Matter* **2016**, *12*, 845; c) S.-J. Park, J. Kim, M. Chu, M. Khine, *Adv. Mater. Technol.* **2016**, *1*, 1600053; d) J. D. Pegan, J. Zhang, M. Chu, T. Nguyen, S.-J. Park, A. Paul, J. Kim, M. Bachman, M. Khine, *Nanoscale* **2016**, *8*, 17295.
[26] a) M. Amjadi, A. Pichitpajongkit, S. Lee, S. Ryu, I. Park, *ACS Nano* **2014**, *8*, 5154; b) N. Lu, C. Lu, S. Yang, J. Rogers, *Adv. Funct. Mater.* **2012**, *22*, 4044; c) T. Yamada, Y. Hayamizu, Y. Yamamoto, Y. Yomogida, A. Izadi-Najafabadi, D. N. Futaba, K. Hata, *Nat. Nanotechnol.* **2011**, *6*, 296; d) Y. R. Jeong, H. Park, S. W. Jin, S. Y. Hong, S.-S. Lee, J. S. Ha, *Adv. Funct. Mater.* **2015**, *25*, 4228; e) J.-H. Kong, N.-S. Jang, S.-H. Kim, J.-M. Kim, *Carbon* **2014**, *77*, 199; f) J. T. Muth, D. M. Vogt, R. L. Truby, Y. Mengüç, D. B. Kolesky, R. J. Wood, J. A. Lewis, *Adv. Mater.* **2014**, *26*, 6307; g) C. S. Boland, U. Khan, C. Backes, A. O'Neill, J. McCauley, S. Duane, R. Shanker, Y. Liu, I. Jurewicz, A. B. Dalton, J. N. Coleman, *ACS Nano* **2014**, *8*, 8819; h) B.-U. Hwang, J.-H. Lee, T. Q. Trung, E. Roh, D.-I. Kim, S.-W. Kim, N.-E. Lee, *ACS Nano* **2015**, *9*, 8801; i) S. Gong, D. T. H. Lai, B. Su, K. J. Si, Z. Ma, L. W. Yap, P. Guo, W. Cheng, *Adv. Electron. Mater.* **2015**, *1*, 1400063; j) E. Roh, B.-U. Hwang, D. Kim, B.-Y. Kim, N.-E. Lee, *ACS Nano* **2015**, *9*, 6252; k) P. Slobodian, P. Riha, P. Saha, *Carbon* **2012**, *50*, 3446; l) P. R. Slobodian, P. Olejnik, R. M. Jiri, *Sens. Rev.* **2018**, *38*, 163; m) S. Tadakaluru, W. Thongsuwan, P. Singjai, *Sensors* **2014**, *14*, 868; n) L. Lin, S. Liu, Q. Zhang, X. Li, M. Ji, H. Deng, Q. Fu, *ACS Appl. Mater. Interfaces* **2013**, *5*, 5815.
[27] S. Timung, J. Chaudhuri, M. P. Borthakur, T. K. Mandal, G. Biswas, D. Bandyopadhyay, *Electrophoresis* **2017**, *38*, 1450.
[28] a) H. Joodaki, M. Panzer, *Proc. Inst. Mech. Eng., Part H* **2018**, *232*, 323; b) A. B. Tepole, A. K. Gosain, E. Kuhl, *Int. J. Non-Linear Mech.* **2012**, *47*, 938.
[29] a) L. J. Hart-Smith, *Z. Angew. Math. Phys.* **1966**, *17*, 608; b) D. Ratna, J. Karger-Kocsis, *J. Mater. Sci.* **2008**, *43*, 254.
[30] a) C. R. Siviour, J. L. Jordan, *J. Dyn. Behav. Mater.* **2016**, *2*, 15; b) A. Kara, A. Tasdemirci, M. Guden, *Mater. Des.* **2013**, *49*, 566.
[31] a) M. Park, J. Im, M. Shin, Y. Min, J. Park, H. Cho, S. Park, M.-B. Shim, S. Jeon, D.-Y. Chung, J. Bae, J. Park, U. Jeong, K. Kim, *Nat. Nanotechnol.* **2012**, *7*, 803; b) J. Li, J.-K. Kim, *Compos. Sci. Technol.* **2007**, *67*, 2114.
[32] S. I. White, R. M. Mutiso, P. M. Vora, D. Jahnke, S. Hsu, J. M. Kikkawa, J. Li, J. E. Fischer, K. I. Winey, *Adv. Funct. Mater.* **2010**, *20*, 2709.
[33] a) V. B. Shenoy, A. F. Schwartzman, L. B. Freund, *Int. J. Fract.* **2001**, *109*, 29; b) Z. C. Xia, J. W. Hutchinson, *J. Mech. Phys. Solids* **2000**, *48*, 1107.
[34] S. G. Yoon, H.-J. Koo, S. T. Chang, *ACS Appl. Mater. Interfaces* **2015**, *7*, 27562.
[35] a) W. Navaraj, R. Dahiya, *Adv. Intell. Syst.* **2019**, *1*, 1900051; b) M. Soni, M. Bhattacharjee, M. Ntagios, R. Dahiya, *IEEE Sens. J.* **2020**, https://doi.org/10.1109/JSEN.2020.2969667.
[36] M. Ntagios, H. Nassar, A. Pullanchiyodan, W. T. Navaraj, R. Dahiya, *Adv. Intell. Syst.* **2019**, *1*, 1900080.

© 2020 The Authors. Published by WILEY-VCH Verlag GmbH & Co. KGaA, Weinheim